


FULL PAPER

Open Access



WS₂–WC–WO₃ nano-hollow spheres as an efficient and durable catalyst for hydrogen evolution reaction

Tuan Van Nguyen¹, Ha Huu Do¹, Mahider Tekalgne¹, Quyet Van Le², Thang Phan Nguyen³, Sung Hyun Hong², Jin Hyuk Cho², Dung Van Dao², Sang Hyun Ahn^{1*} and Soo Young Kim^{2*} 

Abstract

Transition metal dichalcogenides (TMDs), transition metal carbides (TMCs), and transition metal oxides (TMOs) have been widely investigated for electrocatalytic applications owing to their abundant active sites, high stability, good conductivity, and various other fascinating properties. Therefore, the synthesis of composites of TMDs, TMCs, and TMOs is a new avenue for the preparation of efficient electrocatalysts. Herein, we propose a novel low-cost and facile method to prepare TMD–TMC–TMO nano-hollow spheres (WS₂–WC–WO₃ NH) as an efficient catalyst for the hydrogen evolution reaction (HER). The crystallinity, morphology, chemical bonding, and composition of the composite material were comprehensively investigated using X-ray diffraction, Raman spectroscopy, field emission scanning electron microscopy, and X-ray photoelectron spectroscopy. The results confirmed the successful synthesis of the WS₂–WC–WO₃ NH spheres. Interestingly, the presence of nitrogen significantly enhanced the electrical conductivity of the hybrid material, facilitating electron transfer during the catalytic process. As a result, the WS₂–WC–WO₃ NH hybrid exhibited better HER performance than the pure WS₂ nanoflowers, which can be attributed to the synergistic effect of the W–S, W–C, and W–O bonding in the composite. Remarkably, the Tafel slope of the WS₂–WC–WO₃ NH spheres was 59 mV dec^{−1}, which is significantly lower than that of the pure WS₂ NFs (82 mV dec^{−1}). The results also confirmed the unprecedented stability and superior electrocatalytic performance of the WS₂–WC–WO₃ NH spheres toward the HER, which opens new avenues for the preparation of low-cost and highly effective materials for energy conversion and storage applications.

Keywords: TMD, TMC, TMO, WS₂–WC–WO₃ composite, Nano hollow sphere, HER

1 Introduction

Over the past few decades, the over-exploitation of natural resources, such as oil, coal, and fossil gas, has been a critical challenge to humankind [1]. The consequences of the over-use of fossil fuels, including green gas emissions and global warming, have caused a severe threat to the

environment and our lives [2, 3]. Therefore, scientists all over the world have endeavored to develop novel environmentally friendly and facile processes for synthesizing materials suitable for energy storage and conversion applications. Hydrogen is considered as the most efficient fuel [4–6]. The use of hydrogen gas in new technologies has increased significantly because it offers various advantages, such as poison-free gas emission and a simple and scalable production process [7, 8], which involves the application of an electric potential on electrodes in water to split it into oxygen and hydrogen. However, enhancing the efficiency of the water splitting process is a major challenge. In conventional techniques, scarce and

*Correspondence: shahn@cau.ac.kr; sooyoungkim@korea.ac.kr

¹ Department of Chemical and Biological Engineering, Gachon University, Seongnam-si, Gyeonggi-do 13120, Republic of Korea

² Department of Materials Science and Engineering, Institute of Green Manufacturing Technology, Korea University, 145 Anam-ro, Seongbuk-gu, Seoul 02841, Republic of Korea

Full list of author information is available at the end of the article

noble materials, including platinum (Pt) and palladium (Pd), are frequently employed to produce hydrogen gas [9–11]. However, the scarcity, high cost, and poor stability of these noble materials limit their application for the production of hydrogen gas [12]. Therefore, earth-abundant metals have been extensively investigated as catalysts for the hydrogen evolution reaction (HER) [13–15].

Transition metals have partially filled d-orbitals, and hence exhibit unique mechanical and chemical properties, which have been extensively investigated [16, 17]. Interestingly, transition metal dichalcogenide (TMD) materials exhibit impressive electrocatalytic efficiency [18–20] owing to their abundant active sites, earth-abundance, and excellent stability in acidic or basic media [21]. An electrocatalyst should exhibit good conductivity improve the performance of the process [22]. However, the intrinsic conductivity of TMD materials is highly dependent on their morphology, structure, and chemical bonding. TMD materials exhibit poor intrinsic conductivity, which restricts their use in many electrochemical applications [23]. Recently, MoS₂ and WS₂ prepared using various techniques and procedures have been widely investigated for HER applications [24–27]. The different morphologies of WS₂, such as nanosheets, nanoflowers (NFs), nanoparticles, nanotubes, and nanohollow (NH), obtained using different synthesis methods showed different catalytic activities toward hydrogen generation. Nevertheless, the efficiency of these materials still needs to be improved to realize their industrial applications. Transition metal oxides (TMOs) also show various advantages, such as high intrinsic catalytic activity and a variety of desirable physical and chemical properties. The synergistic effect of WS₂ and WO₃ on the HER performance of their composite material has been investigated in detail [28, 29]. At the edge of the art, a new approach to improve the electrocatalytic performance of WS₂ is to combine it with a transition metal carbide (TMC) material, such as WC or MoC [30, 31]. Transition metal carbides (TMCs) show high metallic conductivity and ceramic properties, including chemical durability, high hardness, and high melting point. Recently, TMC materials have been widely used in electrochemical applications owing to their high surface area, excellent electronic conductivity, hydrophilicity, and high chemical and mechanical durability [32, 33].

Herein, we propose a novel strategy to prepare WS₂–WC–WO₃ NH composite materials (WS₂–WC–WO₃ NH). For comparison, WS₂ NFs were also synthesized by slightly modifying the procedure used for synthesizing the WS₂–WC–WO₃ NH spheres. The morphologies, structures, and chemical bonding of both the WS₂–WC–WO₃ NH spheres and WS₂ NFs were investigated various techniques such as X-ray diffraction (XRD), Raman

spectroscopy, field emission scanning electron microscopy (FE-SEM), and X-ray photoelectron spectroscopy (XPS), respectively. The results confirmed the successful preparation of the hybrid NH spheres of WS₂, WC, and WO₃. Interestingly, nitrogen was also detected in the hybrid NH spheres because it was doped in-situ into the hollow composite during the synthesis process. The high HER activity of the hybrid composite can be attributed the presence of WC, WO₃, and nitrogen in it. Nitrogen doping significantly increased the electrical conductivity of the composite. Moreover, the synergistic effect of W–S, W–C, and W–O bonding improved the electrocatalytic performance of the WS₂–WC–WO₃ NH hybrid. Furthermore, the HER electrocatalytic performances of both the WS₂ NFs and WS₂–WC–WO₃ NH spheres were carefully evaluated using a normal three-electrode system. The results showed that the WS₂–WC–WO₃ NH composite is a promising material for next-generation catalysts, which can be employed in energy conversion and storage applications.

2 Experimental details

2.1 Chemical materials

Ammonium meta-tungstate (AMT, (NH₄)₆H₂W₁₂O₄₀) and thioacetamide (TAT, C₂H₅CS, 99%) were purchased from Sigma-Aldrich. Deionized (DI) water was purchased from Millipore Milli-Q system. Absolute ethanol (EtOH, C₂H₅OH) was obtained from Alfa Aesar. All the materials were used as received without further purification.

2.2 Synthesis of the WS₂–WC–WO₃ NH sphere composite

The WS₂–WC–WO₃ NH sphere composite was synthesized using a conventional solvothermal technique. First, 4 g of TAT was dissolved in 20 mL EtOH by stirring at room temperature for 30 min. Then, 4 g of AMT was added to the solution and stirred continuously for another 30 min. The prepared solution was then transferred to a Teflon autoclave for 24 h at 280 °C. The autoclave was then cooled to room temperature. The resulting product was collected and washed with DI water and EtOH three times through centrifugation. Finally, the product was placed in a furnace and dried at 100 °C for 12 h to obtain the WS₂–WC–WO₃ NH composite. Finally, the product was dispersed in DI water by sonication and used for further measurements.

2.3 Synthesis of the WS₂ NFs

The WS₂ NFs were synthesized by slightly modifying the procedure used for the synthesis of the WS₂–WC–WO₃ NH sphere composite. First, 4 g of TAT was dissolved in 20 mL DI water under stirring at room temperature for 30 min. To the resulting mixture, 4 g

of AMT was added and the mixture was stirred continuously for another 30 min. The reaction mixture was then transferred to a Teflon autoclave for 24 h at 200 °C. The autoclave was then cooled to room temperature. The product was collected and washed with DI water and EtOH three times through centrifugation. Then, the product was placed in a furnace and dried at 100 °C for 12 h to obtain the WS₂ NFs. Finally, the product was dispersed in DI water by sonication for further measurements.

2.4 Materials characterization

The crystalline structures of the as-synthesized WS₂ NFs and WS₂-WC-WO₃ NH spheres were analyzed using XRD (D8-Advance/Bruker-AXS). The morphology, size, and shape of the synthesized WS₂ NFs and WS₂-WC-WO₃ NH spheres were analyzed using FE-SEM (SIGMA/Carl Zeiss). Raman spectroscopy (Lab RAM HR, Horiba Jobin Yvon) was performed to investigate the chemical bonding and structure of the materials. The chemical compositions of the WS₂ NFs and WS₂-WC-WO₃ NH spheres were examined using XPS (Thermo Fisher Scientific, K-Alpha, USA) at a base pressure of 1×10^{-5} mbar and 300 K with monochromatic Mg K α radiation (1250 eV) and a constant pass energy of 50 eV.

2.5 Electrochemical measurements

The HER performances of the as-prepared WS₂ NFs and WS₂-WC-WO₃ NH spheres were carefully evaluated using a three-electrode system in a standard 0.5 M H₂SO₄ solution. A carbon rod electrode and a saturated calomel electrode were used as the auxiliary and reference electrodes, respectively. A glassy carbon electrode (GCE) with a diameter of 3 mm was coated with the active material to form the working electrode. The active material was prepared by mixing 2 mg of each sample into 1 mL of DI water and 80 μ L of Nafion (5%) as the stabilizer, followed by sonication for 30 min to form a homogeneous ink. Then, the homogeneous ink was deposited on the surface of the GCE and dried at 80 °C for 30 min. Linear sweep voltammetry (LSV) was performed at a scan rate of 5 mV s⁻¹. To determine the double layer capacitances (C_{dl}) of the samples, the measurements were performed from 0 to 0.2 V at various scan rates of 5, 10, 20, 30, 40, and 50 mV s⁻¹. Electrochemical impedance spectroscopy (EIS) measurements were performed at a potential of -0.33 V vs. RHE over a frequency range of 100 kHz–0.1 Hz. All the potentials were referenced to the reversible hydrogen electrode (RHE) using the Nernst equation: $E_{RHE} = E_{SCE} + E^{\circ}_{SCE} + 0.059 \text{ pH}$.

3 Results and discussion

The XRD patterns of the WS₂-WC-WO₃ NH spheres and WS₂ NFs were obtained to analyze their structures and crystallinity. Figure 1 shows the XRD patterns of the as-prepared WS₂ NFs and WS₂-WC-WO₃ NH spheres. The XRD pattern of the WS₂ NFs showed peaks corresponding to the hexagonal phase of WS₂ (JCPDS Card No. No. 08-0237) [34–36]. The XRD pattern of the WS₂-WC-WO₃ NH spheres showed numerous sharp peaks, indicating the complex growth of different elements. The peaks corresponding to WS₂, WC, and WO₃ could be clearly observed, indicating the coexistence of WS₂, WC, and WO₃ in the composite. This confirms the successful synthesis of the composites of WS₂, WC, and WO₃. The sharp peaks of WS₂, which also appeared in the XRD pattern of the WS₂-WC-WO₃ NH spheres, were located at approximately $2\theta = 14.5^\circ$, 29° , 35.5° , and 60° . The peaks located at approximately $2\theta = 30.5^\circ$, 35.5° , 47° , 63° , 66° , and 71.5° indicate the presence of WC. This is consistent with the results reported previously [37]. The peak observed at $2\theta = 43.5^\circ$ can be attributed to the WC_{1-x} structure [38]. The peaks corresponding to WO₃ were observed at approximately $2\theta = 15^\circ$, 17° , 38° , 51° , and 53° . The results confirmed the existence of the orthorhombic structure of WO₃ in the composite [39, 40]. The XRD pattern of the WS₂ NFs did not show any peak corresponding to WC or WO₃, confirming the successful preparation of pure WS₂. The coexistence of WS₂, WC, and WO₃ in the WS₂-WC-WO₃ NH sphere composite can be attributed to the higher reaction temperature used in the synthesis process than that used in the case of WS₂ NFs. The higher reaction temperature caused the replacement of S elements by C or O elements in the material.

The morphologies of the WS₂-WC-WO₃ NH spheres and WS₂ NFs were carefully observed using FE-SEM, as shown in Fig. 2. The FE-SEM images of the WS₂-WC-WO₃ NH spheres and WS₂ NFs were obtained at various magnifications to clearly observe their sizes, shapes, and morphologies. Figure 2a and c show the SEM images of the highly uniform WS₂ NFs at different scales. The thickness of the NFs ranged from 10 to 20 nm, and the distance between them was approximately 50–150 nm. In contrast, the FE-SEM images of the WS₂-WC-WO₃ composite showed hollow nanospheres. As can be observed from Fig. 2d–f, the diameter of these hollow nanospheres ranged from 300 to 700 nm, and the wall thickness was approximately 30–50 nm. The size of the WS₂-WC-WO₃ NH spheres was much smaller than that of the WS₂ NH spheres reported in a previous study (300 nm–2 μ m) [41]. This indicates that the active sites of the WS₂-WC-WO₃ NH spheres were significantly larger than those of the WS₂ NFs. Interestingly, as can be observed from Fig. 2f, the surface of the WS₂-WC-WO₃

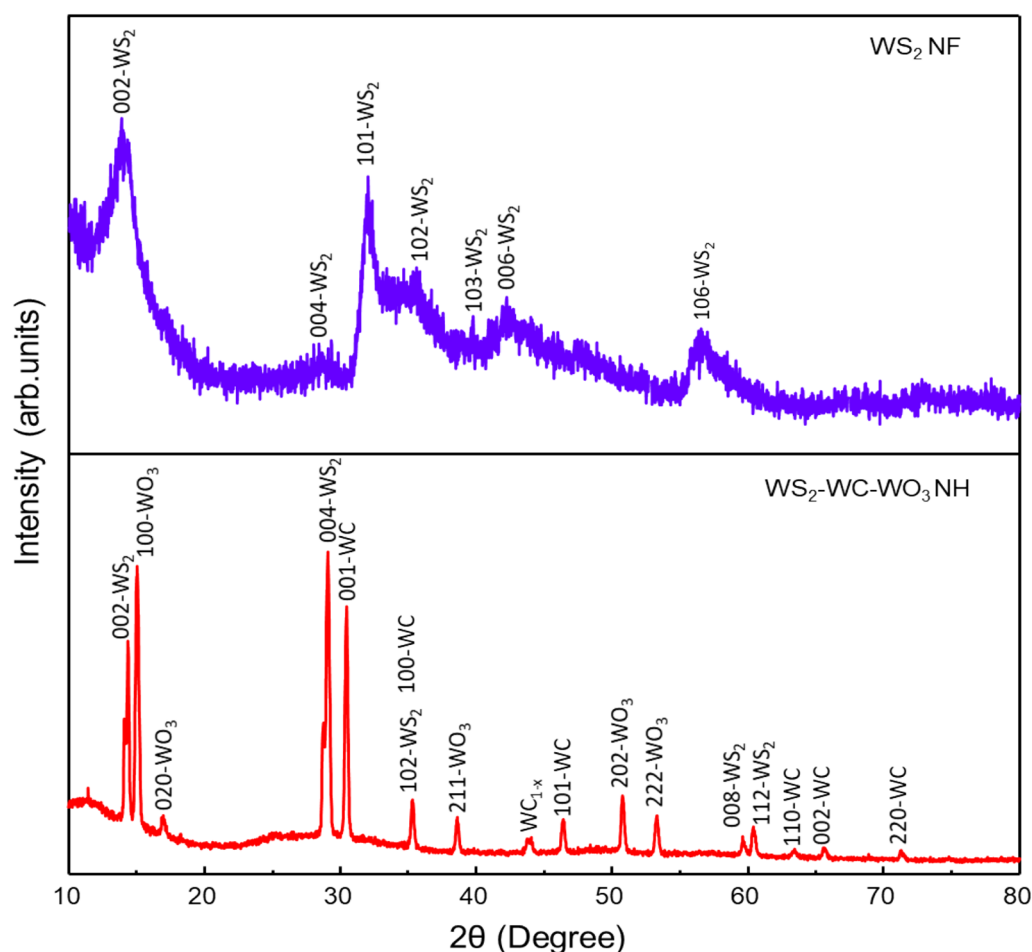


Fig. 1 XRD patterns of the WS_2 NFs and $\text{WS}_2/\text{WC}/\text{WO}_3$ NH spheres

NH spheres was intensively and uniformly cracked. The hollow shape of the material might have been caused by the high synthesis temperature, which created high pressure inside the autoclave. The numerous cracks on the surface of the composite material can be attributed to the decomposition of TAT, in which NH_3 and H_2S gases were released during the sulfurization and carbonization of tungsten in AMT. This resulted in the formation of a hollow structure with numerous cracks on the surface. In addition, the nitrogen released from AMT was trapped in a hollow structure, which caused the in-situ nitrogen doping of the $\text{WS}_2\text{-WC-WO}_3$ NH composite. The EDS mapping of $\text{WS}_2\text{-WC-WO}_3$ NH composite were conducted. The EDS data of $\text{WS}_2\text{-WC-WO}_3$ NH composite was showed in the Additional file 1: Figure S1. The data confirms the well-define spatial elemental distribution for W, S, O, C, N atoms which were 35.24%, 25.32%, 19.53%, 19.41% and 0.45%, respectively. The presence of nitrogen was also detected using XPS. The empty space inside the spheres and the vast cracks on their surface contributed

to the excellent electrocatalytic performance of the $\text{WS}_2\text{-WC-WO}_3$ NH composite by creating a large number of active sites in it. The hollow structure of the material also improved its stability because it prevented the depletion of materials in the electrochemical process.

The chemical structures and bonding of the $\text{WS}_2\text{-WC-WO}_3$ NH spheres and WS_2 NFs were further investigated by obtaining their Raman spectra in Fig. 3. The Raman spectrum of the WS_2 NFs showed bands corresponding to the W-S bonds at 352 and 417 cm^{-1} . These bonds were related to the weak van der Waals interlayer interactions affecting the intralayer bonding and lattice vibration of stacked layer crystallites [42, 43]. These bands belong to the E_{2g} mode of the W+S movement in the x-y plane and the A_{1g} mode of the S movement along the z-axis [44, 45]. The Raman spectrum of the WS_2 NFs showed peaks corresponding to WO_3 at 131.3 , 180 , 261.9 , 695 , and 805 cm^{-1} , which resulted in the surface oxidation of WS_2 . The Raman spectrum of the $\text{WS}_2\text{-WC-WO}_3$ NH spheres showed two peaks corresponding

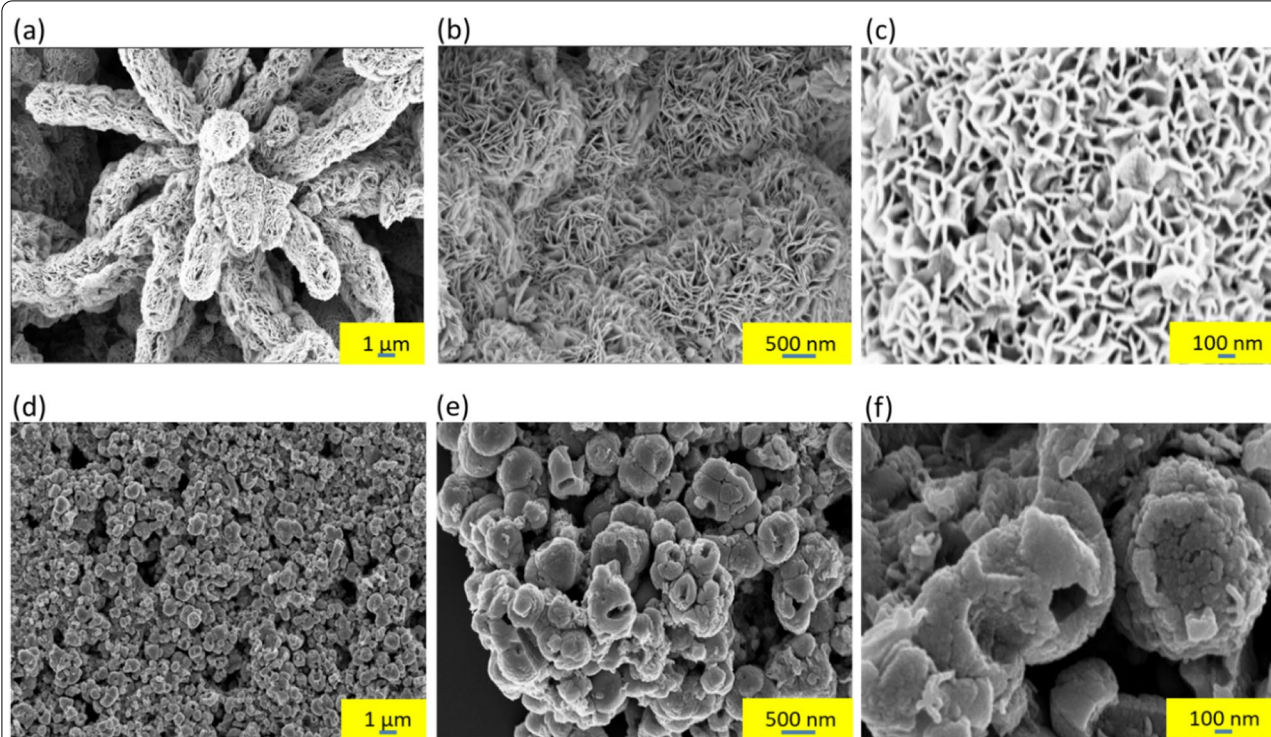


Fig. 2 FE-SEM images of **a–c** the WS_2 NFs and **d–f** $\text{WS}_2\text{-WC-WO}_3$ NH spheres at different scales

to WS_2 at approximately 352 and 417 cm^{-1} . The Raman peaks corresponding to WO_3 could be clearly observed at 131.3 , 185 , 261.9 , 327 , 695 , and 805 cm^{-1} . The sharp WO_3 peak centered at 327 cm^{-1} marked the most significant difference between the Raman spectra of the two materials. This peak indicates the co-existence of WO_3 , WS_2 , and WC in the composite materials. The band at 695 cm^{-1} corresponds to the O–W–O stretching mode of WO_3 , while that at 805 cm^{-1} could be ascribed to the asymmetric stretching mode of oxygen bridge (O–W–O). These O–W–O bands existed because the composite exhibited basal plane orientations that were perpendicular to the substrate surface. The Raman spectrum of the $\text{WS}_2\text{-WC-WO}_3$ NH spheres showed broad bands at approximately 1393 and 1594 cm^{-1} corresponding to WC [38]. Interestingly, the Raman peaks corresponding to WC were observed at approximately 262 , 329 , 710.8 , and 807.2 cm^{-1} . These peak positions were quite overlapping as compared to those of WO_3 [46].

The elemental compositions of the WS_2 NFs and $\text{WS}_2\text{-WC-WO}_3$ NH spheres were further investigated by carrying out XPS measurements, as shown in Fig. 4. The wide XPS survey profiles of the WS_2 NFs and $\text{WS}_2\text{-WC-WO}_3$ NH spheres are shown in Fig. 4a. As can be observed from the figure, the XPS profiles of both the WS_2 NFs and $\text{WS}_2\text{-WC-WO}_3$ NH spheres showed

nitrogen peaks, indicating that nitrogen was doped in-situ into the WS_2 NFs and $\text{WS}_2\text{-WC-WO}_3$ NH spheres during the synthesis process. This is contrary to the results of a previous study, in which the nitrogen doping of the catalytic material was not observed [24]. The appearance of nitrogen was caused by the use of AMT as the precursor during the synthesis. The presence of nitrogen in the $\text{WS}_2\text{-WC-WO}_3$ NH composite significantly improved its conductivity and electrocatalytic performance [47]. The significant differences in the chemical composition and the W 4f binding energy levels of the WS_2 NFs and $\text{WS}_2\text{-WC-WO}_3$ NH spheres can be clearly observed from Fig. 4b and c. As can be observed from Fig. 4b, the W 4f profile of the $\text{WS}_2\text{-WC-WO}_3$ NH spheres showed peaks corresponding to W–C, W–S, and W–O [48] because of the presence of WS_2 , WC, and WO_3 . The synergistic effect of these components improved the material characteristics, leading to a significant improvement in its HER performance as compared to that of the bare WS_2 [49]. In Fig. 4c, The W 4f XPS profile of the WS_2 NFs showed only the peaks corresponding to W–S and W–O, which originated from surface oxidation of WS_2 (Fig. 4c). The peaks located at approximately 32 and 34.2 eV could be assigned to the W $4f_{7/2}$ and W $4f_{5/2}$ levels of the W–S bonds, while peaks located at 35.6 and 37.8 eV

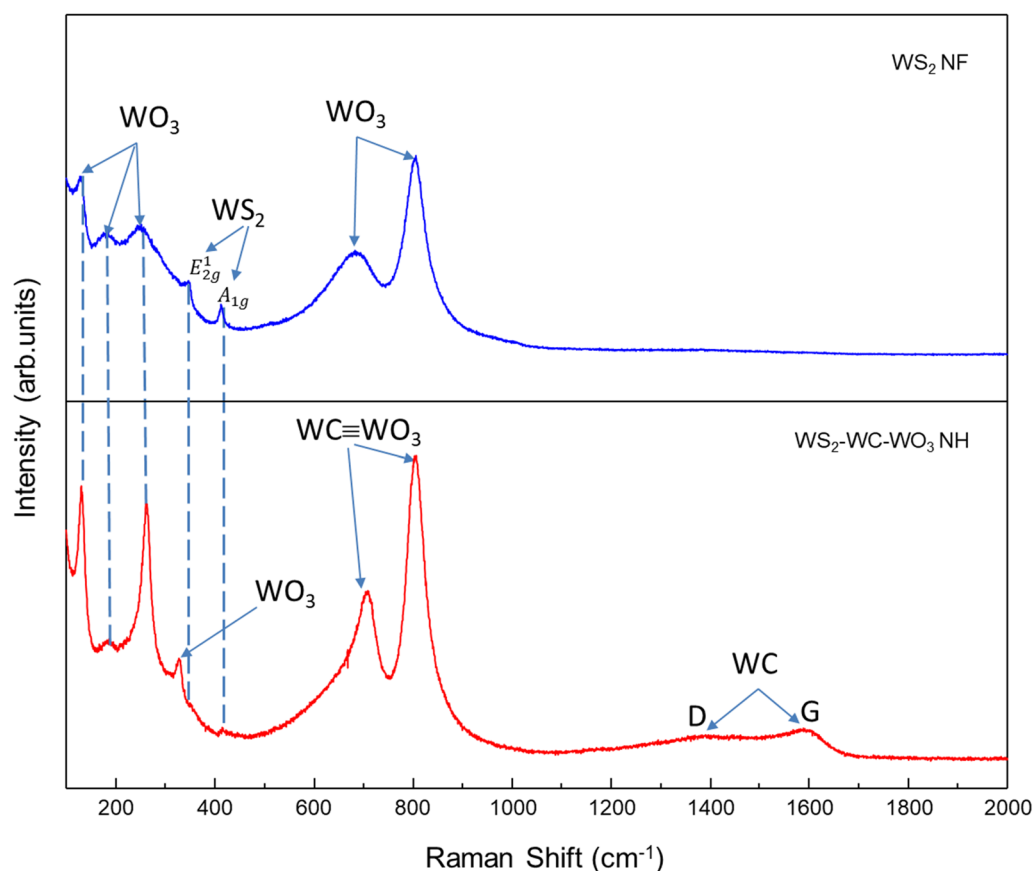
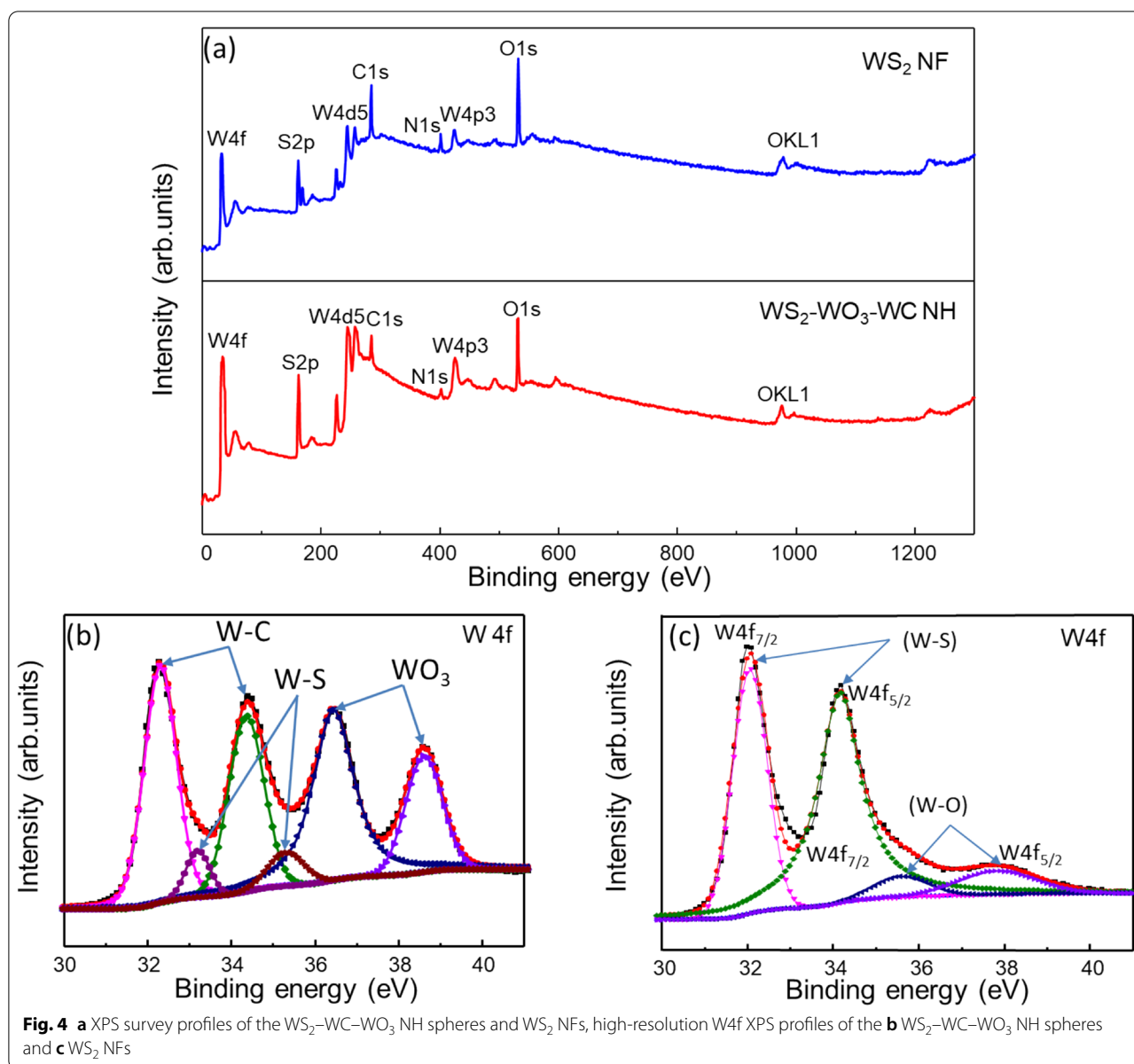


Fig. 3 Raman spectra of the WS_2 NFs and $\text{WS}_2\text{-WC-WO}_3$ NH spheres

corresponded to the $\text{W } 4f_{7/2}$ and $\text{W } 4f_{5/2}$ levels of W-O bonding. The core-level XPS profiles of the WS_2 NFs and $\text{WS}_2\text{-WC-WO}_3$ NH spheres are shown in Additional file 1: Figures S2 and S3, respectively. Both the samples showed high-resolution $\text{C } 1s$ and $\text{O } 1s$ peaks. However, in the XPS profiles of the WS_2 NFs, the oxygen peaks were detected because of the surface oxidation of WS_2 , while the carbon peaks were attributed to the graphitic TAT used in the synthesis process. This is consistent with the XRD and Raman spectroscopy results. The $\text{S } 2p$, $\text{N } 1s$, and $\text{O } 1s$ PS profiles of the WS_2 NFs are shown in Additional file 1: Figure S2a–c. In contrast, the oxygen and carbon peaks in the XPS profile of the $\text{WS}_2\text{-WC-WO}_3$ NH spheres indicate the co-existence of WC and WO_3 . The co-existence of WC and WO_3 in the $\text{WS}_2\text{-WC-WO}_3$ NH composite was also indicated by the XRD and Raman spectroscopy results. To understand the complex peaks of the other elements on the surface of the materials, the $\text{S } 2p$, $\text{N } 1s$, $\text{O } 1s$ and $\text{C } 1s$ peaks of the $\text{WS}_2\text{-WC-WO}_3$ NH composite were deconvoluted, as shown in Additional file 1: Figure S3a–d. The $\text{S } 2p$ peaks of the WS_2 NFs and

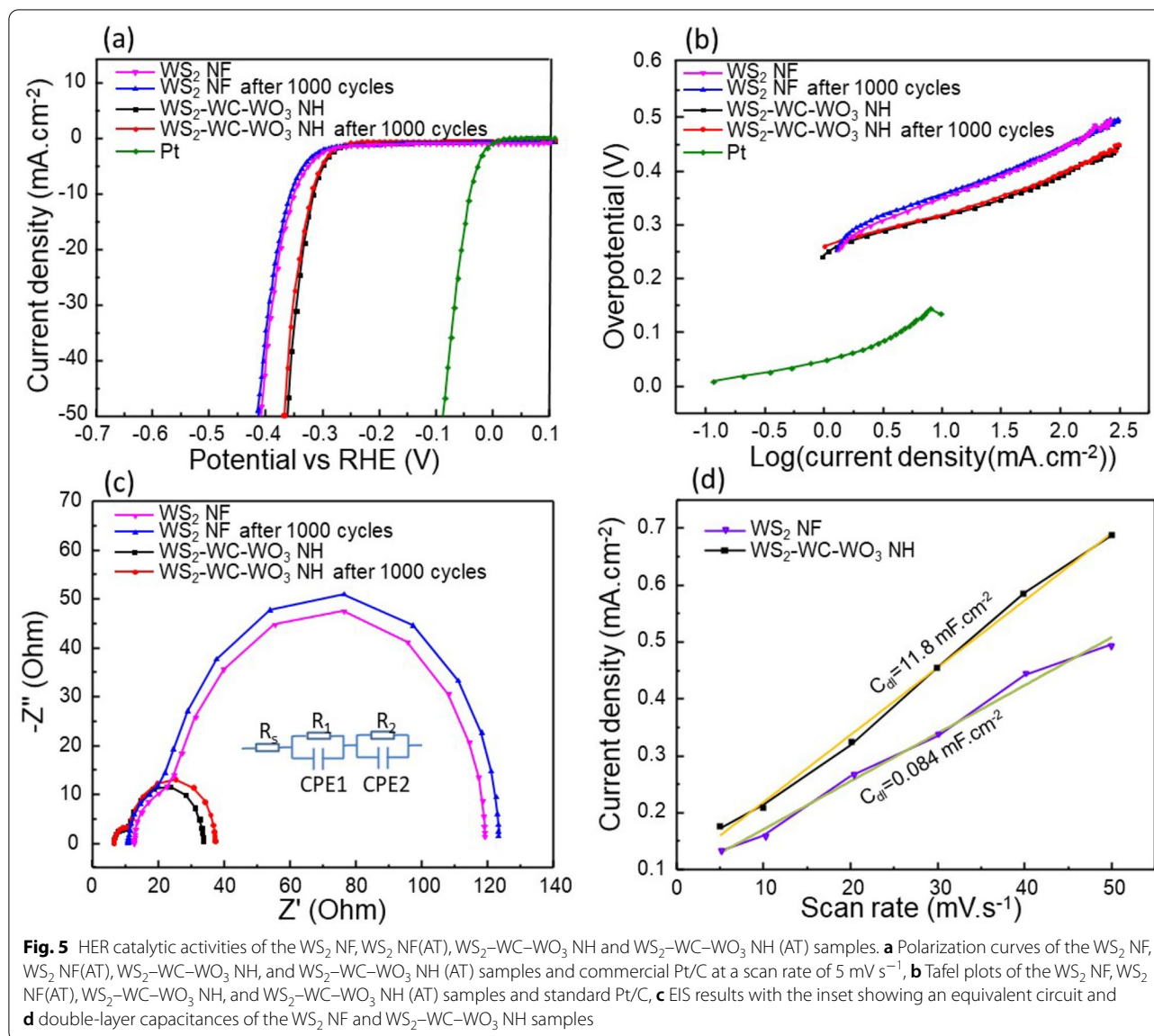
$\text{WS}_2\text{-WC-WO}_3$ NH spheres were also significantly different. The $\text{S } 2p$ peak of the $\text{WS}_2\text{-WC-WO}_3$ NH composite could be deconvoluted into three main peaks located at approximately 161.9, 163.2, and 164.5 eV corresponding to the $\text{S } 2p_{3/2}$ and $\text{S } 2p_{1/2}$ orbitals of divalent sulfide ions and C-S=C bonding, respectively, as shown in Additional file 1: Figure S3a. In contrast, as shown in Additional file 1: Figure S2a the $\text{S } 2p$ peak of the WS_2 NFs could be deconvoluted into two main peaks centered at 161.6 and 163 eV corresponding to the $\text{S } 2p_{3/2}$ and $\text{S } 2p_{1/2}$ orbitals of divalent sulfide ions, respectively [50]. The $\text{N } 1s$ XPS peak of the $\text{WS}_2\text{-WC-WO}_3$ NH composite could be deconvoluted into two components centered at approximately 400.1 and 402.8 eV, corresponding to free nitrogen and hydrogen bonding amine, respectively (Additional file 1: Figure S3b) [51]. The $\text{O } 1s$ peak of the $\text{WS}_2\text{-WC-WO}_3$ NH composite could be deconvoluted into $-\text{O}-$ and $-\text{OH}$ peaks, which were attributed to surface contamination and O^{2-} combined with W ions, respectively [52]. The $\text{C } 1s$ peak could be deconvoluted into several peaks, as shown in Additional file 1: Figure S3d. We focused



on the two strongest peaks centered at approximately 284.8 and 286 eV corresponding to the sp^2 and sp^3 hybridization of the C-C or C-H bonds, respectively [53].

The HER performances of the WS₂ NFs and WS₂-WC-WO₃ NH spheres were carefully investigated using a three-electrode system (Fig. 5). The HER performance of the WS₂ NFs was highly consistent with that obtained in our previous study [41]. The Tafel slope, impedance, and double-layer capacitance of the WS₂ NFs were approximately 82 mV dec⁻¹, 95 Ω, and 0.08 mF cm⁻², respectively. To drive a cathodic current density of -10 mA cm⁻², an overvoltage of -352 mV was employed. The

stability of WS₂ NFs was tested for 1000 cycles, the polarization curves of tested samples was carried out. The HER performance of WS₂ NFs after test (AT) was presented in Fig. 5. After stability test, the Tafel slope of WS₂ NFs AT was increased from 82 mV dec⁻¹ to 83.5 mV dec⁻¹. The data indicates that WS₂ NFs is quite stable in acid media for HER application with a negligible shift after stability test. We also investigated the HER performance of the WS₂-WC-WO₃ NH spheres before and after test (WS₂-WC-WO₃ NH (AT))-the stability test using cyclic voltammetry (1000 cycles), which was denoted as WS₂-WC-WO₃ NH (AT). The electrocatalytic activity of the WS₂-WC-WO₃ NH composite toward the HER was



measured using a three-electrode system in a standard acidic medium of $0.5 \text{ M H}_2\text{SO}_4$. The stability the $\text{WS}_2\text{-WC-WO}_3$ NH composite was evaluated over the overpotential range of -0.3 to -0.5 V for 1000 cycles, as shown in Additional file 1: Figure S5b. Figure 5a shows the polarization curves of the WS_2 NF, $\text{WS}_2\text{-WC-WO}_3$ NH, and $\text{WS}_2\text{-WC-WO}_3$ NH (AT) samples and a standard platinum electrode. After 1000 cycles, the overpotential of the $\text{WS}_2\text{-WC-WO}_3$ NH sample decreased slightly as compared to the initial value, indicating the outstanding durability of the sample. At the current density of -10 mA cm^{-2} , the overpotential of the $\text{WS}_2\text{-WC-WO}_3$ NH

sample was -0.312 mV , which is much better than that of the WS_2 NFs (-352 mV). Therefore, the $\text{WS}_2\text{-WC-WO}_3$ NH composite is a promising material for water dissociation as compared to the WS_2 NFs. To further evaluate the HER performances of the $\text{WS}_2\text{-WC-WO}_3$ NH and $\text{WS}_2\text{-WC-WO}_3$ NH (AT) samples in acidic media, their Tafel slopes were plotted, as shown in Fig. 5b. The Tafel slopes of the $\text{WS}_2\text{-WC-WO}_3$ NH and $\text{WS}_2\text{-WC-WO}_3$ NH (AT) samples were 59 and 60 mV dec^{-1} , respectively. This confirms that the stability of the $\text{WS}_2\text{-WC-WO}_3$ NH material was much better than that of the WS_2 NFs (82 mV dec^{-1}). Figure 5c shows the electronic properties

Table 1 The fitting values of charge-transfer resistances (R_s), the resistance between the electrocatalysts and solution (R_1), and the resistance between the electrocatalysts and GCE (R_2) of samples

	R_s (Ω)	R_1 (Ω)	R_2 (Ω)
WS ₂ -WC-WO ₃ NH	6.44	22.94	4.271
WS ₂ -WC-WO ₃ NH (AT)	6.47	25.91	4.89
WS ₂ NF	12.69	94.36	12.22
WS ₂ NF (AT)	12.74	98.25	13.01

of the materials before and after the cyclic voltammetry (CV) test. The equivalent circuit shown in the inset of Fig. 5c was composed of constant phase elements and charge-transfer resistances. The charge-transfer resistances included the wire connection (R_s), the resistance between the electrocatalysts and solution (R_1), and the resistance between the electrocatalysts and GCE (R_2). The fitting values are listed in Table 1. The connection showed a resistance of 6.44–6.47 Ω . More importantly, the charge transfer resistance of the WS₂-WC-WO₃ NH composite was approximately 22.94 Ω , indicating that the electron conduction on the surface of the hollow composite was better than that of the pure WS₂ NFs (94.36 Ω). This means that the conductivity of the WS₂-WC-WO₃ NH composite was much higher than that of the WS₂ NFs. The double-layer capacitance (C_{dl}) of the WS₂-WC-WO₃ NH composite and WS₂ NFs was calculated via CV scanning at different scan rates of 5, 10, 20, 30, 40, and 50 mV s⁻¹. The CV curves were obtained within the potential window of 0–0.2 V, where no Faradaic current was observed. The CV scans of the WS₂ NF and WS₂-WC-WO₃NH samples at various scan rates are shown in Additional file 1: Figures S4a and S5a, respectively. Figure 5d shows that the C_{dl} of the WS₂-WC-WO₃ NH and WS₂ NF samples were approximately 11.8 mF cm⁻² and 0.084 mF cm⁻², respectively. The higher C_{dl} of the WS₂-WC-WO₃ NH composite can be attributed to its hollow sphere structure, owing to which it had a larger active surface and was robust to surface depletion during the electrochemical process. Additional file 1: Table S1 presents this work results and previous data. It indicates that WS₂-WC-WO₃ NH is a prominent catalyst material which could be applied for HER application.

Another important parameter affecting the electrochemical performance of a material is its electrochemical active surface area (ECSA). ECSA represents the area of an electrode material that is accessible to the solution for electron transfer or charge storage. The ECSA of an electrode can be calculated using the following equations [54, 55]:

$$ECSA = \frac{C_{dl}}{C_s} \quad (1)$$

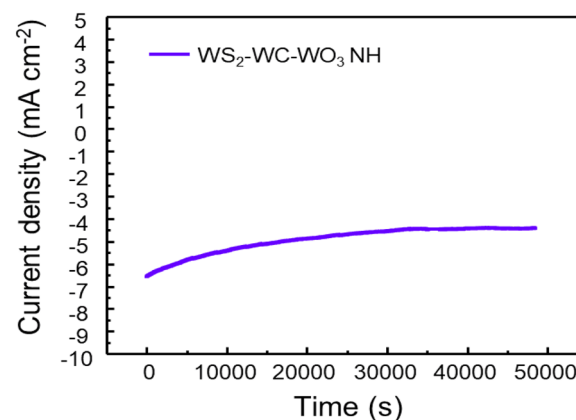
where C_s is the capacitance per unit area of the smooth planar surface of the material. Here we used a general specific capacitance of $C_s = 0.04$ mF/cm² in 0.5 M H₂SO₄. The C_{dl} values of the WS₂-WC-WO₃NH and WS₂ NF samples were calculated to be 11.8 and 0.084 mF cm⁻², respectively. By substituting the values of C_{dl} and C_s in Eq. (1), the ECSA values of the WS₂-WC-WO₃ NH and WS₂ NF samples were calculated to be 295 and 2.1, respectively. These values indicate that the WS₂-WC-WO₃ NH composite showed better charge transfer or charge storage than the WS₂ NFs.

The turnover frequency (TOF) of H₂ is the number of H₂ molecules generated per active site per unit time. The TOF of H₂ produced by the WS₂ NFs and WS₂-WC-WO₃ NH spheres was calculated using the following formula [56, 57].

$$TOF = \frac{jA}{4nF} \quad (2)$$

where j is the current density (A cm⁻²), A is the surface area of the working electrode (cm²), n is the number of moles of the catalyst loaded onto the working electrode, and F is the faraday constant ($F = 96485.3329$ C mol⁻¹). The TOFs of H₂ production at $\eta = -312$ mV and -352 mV (current density measured = 10 mA cm⁻²) for the WS₂ NF and WS₂-WC-WO₃ NH samples were 0.08 and 0.02 s⁻¹, respectively, and the corresponding results are shown in Additional file 1: Figures S4b and S5c.

Finally, the stability of the WS₂-WC-WO₃ NH spheres was also investigated by prolonged electrolysis at a constant overpotential of -0.33 V. As can be observed from Fig. 6, the sample showed excellent

**Fig. 6** Time-dependent current density of the WS₂-WC-WO₃NH spheres at -0.33 V for 50,000 s

stability in a 0.5 M H₂SO₄ solution for 50,000 s. The results indicate that the composite prepared in this study is a promising material for electrochemical applications.

4 Conclusions

In this study, we developed a facile and low-cost procedure to prepare a novel composite of WS₂ (TMD), WC (TMC), and WO₃ (TMO) (WS₂-WC-WO₃ NH) using the conventional solvothermal technique. Interestingly, the hybrid material was doped in-situ with nitrogen. The electrochemical measurements of the WS₂-WC-WO₃NH composite were also carried out in an acidic medium to evaluate its electrocatalytic performance for the HER. The results indicated that the WS₂-WC-WO₃ NH composite exhibited extraordinary electrocatalytic properties as compared to the pure WS₂ NFs. This improvement can be attributed to the presence of WC and WO₃, which exhibited a synergistic effect with WS₂ and endowed the composite with various advantages of TMC and TMO materials. Moreover, the nitrogen doping significantly increased the electrical conductivity of the hybrid material. The Tafel slopes of the WS₂-WC-WO₃ NH composite before and after the CV test (1000 cycles) were 59 and 60 mV dec⁻¹, respectively. These results demonstrate the excellent performance and stability of the WS₂-WC-WO₃ NH catalyst for the HER. Therefore, the WS₂-WC-WO₃ NH composite prepared in this study is a promising alternative to expensive noble metal catalysts for the HER and other electrochemical applications.

Abbreviations

NH: Nano-hollow; NF: Nanoflower; HER: Hydrogen evolution reaction; TMD: Transition metal dichalcogenide; TMO: Transition metal oxide; TMC: Transition metal carbide; FE-SEM: Field emission scanning electron microscopy; XRD: X-ray diffraction; XPS: X-ray photoelectron spectroscopy; CV: Cyclic voltammetry; EIS: Electrochemical impedance spectroscopy; AMT: Ammonium metatungstate; TAT: Thioacetamide; DI: De-ionized; GCE: Glassy carbon electrode; LSV: Linear sweep voltammetry; RHE: Reference hydrogen electrode; ECSA: Electrochemical active surface area; TOF: Turnover frequency.

Supplementary Information

The online version contains supplementary material available at <https://doi.org/10.1186/s40580-021-00278-3>.

Additional file 1: Figure S1. EDS map images of WS₂-WC-WO₃ NH spheres showing the spatial elemental distribution for W, S, O, C and N atoms. **Figure S2.** High-resolution (a) S 2p, (b) N 1s, and (c) O 1s XPS profiles of the WS₂ NFs. **Figure S3.** High-resolution (a) S 2p, (b) N 1s, (c) O 1s, and (d) C 1s XPS profiles of the WS₂-WC-WO₃ NH spheres. **Figure S4.** (a) CV curves and (b) TOF of the WS₂ NFs. **Figure S5.** CV curves of the WS₂-WC-WO₃ NH composite at various scan rates (a) before and (b) after 1000 cycles and (c) TOF of the WS₂-WC-WO₃ NH composite. **Table S1.** Comparison of other electrocatalysts previously reported in HER.

Acknowledgements

Not applicable.

Authors' contributions

TVN and HHD prepared experiment and wrote the original manuscript. MT, SHH, JHC measured XRD, FE-SEM, Raman and XPS. QVL, TPN, DVD interpreted all the data of manuscript. SHA, SYK performed the data curation, overall review of the manuscript and funding acquisition. All authors read and approved the final manuscript.

Funding

This research was supported by a National Research Foundation of Korea (NRF) grant funded by the Korean government (MSIT) (2021R1A4A3027878, 2020H1D3A1A04081409).

Availability of data and materials

The datasets used and/or analyzed during the current study are available from the corresponding author upon reasonable request.

Declarations

Competing interests

The authors declare that they have no competing interests.

Author details

¹Department of Chemical and Biological Engineering, Gachon University, Seongnam-si, Gyeonggi-do 13120, Republic of Korea. ²Department of Materials Science and Engineering, Institute of Green Manufacturing Technology, Korea University, 145 Anam-ro, Seongbuk-gu, Seoul 02841, Republic of Korea. ³Department of Chemical and Biological Engineering, Gachon University, Seongnam-si, Gyeonggi-do 13120, Republic of Korea.

Received: 21 July 2021 Accepted: 2 September 2021

Published online: 20 September 2021

References

- M.L. Khandekar, T. Murty, P. Chittibabu, The global warming debate: a review of the state of science. *Pure Appl. Geophys.* **162**, 1557–1586 (2005)
- W. Bach, Fossil fuel resources and their impacts on environment and climate. *Int. J. Hydrogen Energy.* **6**, 185–201 (1981)
- J. Bebbington, T. Schneider, L. Stevenson, A. Fox, Fossil fuel reserves and resources reporting and unburnable carbon: investigating conflicting accounts. *Crit. Perspect. Account.* **66**, 102083 (2020)
- J.O. Abe, A. Popoola, E. Ajenifuja, O. Popoola, Hydrogen energy, economy and storage: review and recommendation. *Int. J. Hydrogen Energy.* **44**, 15072–15086 (2019)
- C. Acar, I. Dincer, Review and evaluation of hydrogen production options for better environment. *J. Clean. Prod.* **218**, 835–849 (2019)
- I. Staffell, D. Scamman, A.V. Abad, P. Balcombe, P.E. Dodds, P. Ekins, N. Shah, K.R. Ward, The role of hydrogen and fuel cells in the global energy system. *Energy Environ. Sci.* **12**, 463–491 (2019)
- T. He, P. Pachfule, H. Wu, Q. Xu, P. Chen, Hydrogen carriers. *Nat. Rev. Mater.* **1**, 1–17 (2016)
- M. Navlani-García, K. Mori, Y. Kuwahara, H. Yamashita, Recent strategies targeting efficient hydrogen production from chemical hydrogen storage materials over carbon-supported catalysts. *NPG Asia Mater.* **10**, 277–292 (2018)
- C. Li, J.B. Baek, Recent advances in noble metal (Pt, Ru, and Ir)-based electrocatalysts for efficient hydrogen evolution reaction. *ACS Omega.* **5**, 31–40 (2019)
- J. Fan, K. Qi, L. Zhang, H. Zhang, S. Yu, X. Cui, Engineering Pt/Pd interfacial electronic structures for highly efficient hydrogen evolution and alcohol oxidation. *ACS Appl. Mater. Interfaces.* **9**, 18008–18014 (2017)
- S. Sarkar, S.C. Peter, An overview on Pd-based electrocatalysts for the hydrogen evolution reaction. *Inorg. Chem. Front.* **5**, 2060–2080 (2018)

12. X. Ren, Q. Lv, L. Liu, B. Liu, Y. Wang, A. Liu, G. Wu, Current progress of Pt and Pt-based electrocatalysts used for fuel cells. *Sustain. Energy Fuels*. **4**, 15–30 (2020)
13. T. Shan-Shan, W. Xue-Jing, L. Qing-Chuan, Xiao-Jun, Progress on electrocatalysts of hydrogen evolution reaction based on carbon fiber materials. *Chin. J. Anal. Chem.* **44**, 1447–1457 (2016)
14. Y. Wu, H. He, Electrodeposited nickel–iron–carbon–molybdenum film as efficient bifunctional electrocatalyst for overall water splitting in alkaline solution. *Int. J. Hydrogen Energy*. **44**, 1336–1344 (2019)
15. A. Borgschulte, O. Sambalova, R. Delmelle, S. Jenatsch, R. Hany, F. Nüesch, Hydrogen reduction of molybdenum oxide at room temperature. *Sci. Rep.* **7**, 1–9 (2017)
16. J. Kim, M. Kim, C.Y. Seo, J. Ryu, T. Ryu, H.-J. Hong, D. Shin, Y.J. Suh, Effects of Al, V, Cr, Mn, Ni, Nb, Mo, and W Addition to BCC-Fe on its elastic properties and hardness for a biomass boiler: First principles approaches. *Korean J Metals Mater.* **57**, 374–380 (2019)
17. M.J. Kim, S.H. Bak, J. Hahn, S.J. Kim, D.B. Lee, High-temperature oxidation of Fe₁₂Cr_{0.3}C₄Mn_(13–15)Cu composite alloys. *Korean J. Metals Mater.* **57**, 575–581 (2019)
18. K. Zhu, C. Li, Z. Jing, X. Liu, Y. He, X. Lv, Y. Wang, K. Liu, Two-dimensional transition-metal dichalcogenides for electrochemical hydrogen evolution reaction. *FlatChem*. **18**, 100140 (2019)
19. X. Chia, M. Pumera, Characteristics and performance of two-dimensional materials for electrocatalysis. *Nat. Catal.* **1**, 909–921 (2018)
20. D.R. Cummins, U. Martinez, A. Sherehiy, R. Kappera, A. Martinez-Garcia, R.K. Schulze, J. Jasinski, J. Zhang, R.K. Gupta, J. Lou, Efficient hydrogen evolution in transition metal dichalcogenides via a simple one-step hydrazine reaction. *Nat. Commun.* **7**, 1–10 (2016)
21. W. Choi, N. Choudhary, G.H. Han, J. Park, D. Akinwande, Y.H. Lee, Recent development of two-dimensional transition metal dichalcogenides and their applications. *Mater. Today*. **20**, 116–130 (2017)
22. H. Schmidt, F. Giustiniano, G. Eda, Electronic transport properties of transition metal dichalcogenide field-effect devices: surface and interface effects. *Chem. Soc. Rev.* **44**, 7715–7736 (2015)
23. B. Chen, G. Sun, J. Wang, G. Liu, C. Tan, Y. Chen, H. Cheng, J. Chen, Q. Ma, L. Huang, Transition metal dichalcogenide/multi-walled carbon nanotube-based fibers as flexible electrodes for electrocatalytic hydrogen evolution. *Chem. Commun.* **56**, 5131–5134 (2020)
24. T.P. Nguyen, S.Y. Kim, T.H. Lee, H.W. Jang, Q. Van Le, I.T. Kim, Facile synthesis of W₂C@WS₂ alloy nanoflowers and their hydrogen generation performance. *Appl. Surf. Sci.* **504**, 144389 (2020)
25. A. Hasani, T.P. Nguyen, M. Tekalgne, Q. Van Le, K.S. Choi, T.H. Lee, T.J. Park, H.W. Jang, S.Y. Kim, The role of metal dopants in WS₂ nanoflowers in enhancing the hydrogen evolution reaction. *Appl. Catal. A General*. **567**, 73–79 (2018)
26. X. Liu, L. Liu, Y. Wu, Y. Wang, J. Yang, Z. Wang, Rosette-like MoS₂ nanoflowers as highly active and stable electrodes for hydrogen evolution reactions and supercapacitors. *RSC Adv.* **9**, 13820–13828 (2019)
27. X. Ren, F. Yang, R. Chen, P. Ren, Y. Wang, Improvement of HER activity for MoS₂: insight into the effect and mechanism of phosphorus post-doping. *New J. Chem.* **44**, 1493–1499 (2020)
28. X. Shang, Y. Rao, S.S. Lu, B. Dong, L.M. Zhang, X.H. Liu, X. Li, Y.R. Liu, Y.M. Chai, C.G. Liu, Novel WS₂/WO₃ heterostructured nanosheets as efficient electrocatalyst for hydrogen evolution reaction. *Mater. Chem. Phys.* **197**, 123–128 (2017)
29. N. Lee, J. Kwak, J.H. Kwak, S.-M. Jung, J. Kim, A. Giri, K. Thiyagarajan, Y.T. Kim, S. Jung, J.K. Kim, Microwave-assisted evolution of WO₃ and WS₂/WO₃ hierarchical nanotrees. *J. Mater. Chem. A*. **8**, 9654–9660 (2020)
30. M. Shi, Z. Jiang, B. Mei, Y. Li, F. Sun, H. Yu, Y. Xu, Tuning the hydrogen evolution performance of 2D tungsten disulfide by interfacial engineering. *J. Mater. Chem. A*. **9**, 7059–7067 (2021)
31. P. Yan, Y. Wu, X. Wei, X. Zhu, W. Su, Preparation of robust hydrogen evolution reaction electrocatalyst WC/C by molten salt. *Nanomaterials*. **10**, 1621 (2020)
32. J. Huang, W. Hong, J. Li, B. Wang, W. Liu, High-performance tungsten carbide electrocatalysts for the hydrogen evolution reaction. *Sustain. Energy Fuels*. **4**, 1078–1083 (2020)
33. C. Liu, D. Zhou, J. Zhou, Z. Xie, Y. Xia, Synthesis and characterization of tungsten carbide and application to electrocatalytic hydrogen evolution. *RSC Adv.* **6**, 76307–76311 (2016)
34. X. Zhang, H. Tan, Z. Fan, M. Ge, X. Ye, M. Xue, Synthesis and electrochemical performance of ultrathin WS₂ nanosheets. *Chalcogenide Letters*. **14**, (2017)
35. X. Zhang, H. Xu, J. Wang, X. Ye, W. Lei, M. Xue, H. Tang, C. Li, Synthesis of ultrathin WS₂ nanosheets and their tribological properties as lubricant additives. *Nanoscale Res. Lett.* **11**, 1–9 (2016)
36. Y. Zhu, W. Hsu, H. Terrones, N. Grobert, B. Chang, M. Terrones, B. Wei, H. Kroto, D. Walton, C. Boothroyd, Morphology, structure and growth of WS₂ nanotubes. *J. Mater. Chem.* **10**, 2570–2577 (2000)
37. M. Shi, L. Kang, Y. Jiang, Microwave-assisted synthesis of mesoporous tungsten carbide/carbon for fuel cell applications. *Catal. Lett.* **144**, 278–284 (2014)
38. A. Pawbake, R. Waykar, A. Jadhavar, R. Kulkarni, V. Waman, A. Date, D. Late, H. Pathan, S. Jadhav, Wide band gap and conducting tungsten carbide (WC) thin films prepared by hot wire chemical vapor deposition (HW-CVD) method. *Mater. Lett.* **183**, 315–317 (2016)
39. R. Balzer, V. Drago, W.H. Schreiner, L.F. Probst, Synthesis and structure-activity relationship of a WO₃ catalyst for the total oxidation of BTX. *J. Brazil. Chem. Soc.* **25**, 2026–2031 (2014)
40. A.V. Kadam, S.B. Patil, Polyaniline globules as a catalyst for WO₃ nanoparticles for supercapacitor application. *Mater. Res. Express*. **5**, 085036 (2018)
41. T.P. Nguyen, D.L.T. Nguyen, V.H. Nguyen, T.H. Le, Q.V. Ly, D.V.N. Vo, Q.V. Nguyen, H.S. Le, H.W. Jang, S.Y. Kim, Facile synthesis of WS₂ hollow spheres and their hydrogen evolution reaction performance. *Appl. Surf. Sci.* **505**, 144574 (2020)
42. G. Frey, R. Tenne, M. Matthews, M. Dresselhaus, G. Dresselhaus, Optical properties of MS₂ (M = Mo, W) inorganic fullerene-like and nanotube material optical absorption and resonance Raman measurements. *J. Mater. Res.* **13**, 2412–2417 (1998)
43. S. Li, Z. Chen, W. Zhang, Dye-sensitized solar cells based on WS₂ counter electrodes. *Mater. Lett.* **72**, 22–24 (2012)
44. N.D. Boscher, C.J. Carmalt, I.P. Parkin, Atmospheric pressure chemical vapor deposition of WSe₂ thin films on glass—highly hydrophobic sticky surfaces. *J. Mater. Chem.* **16**, 122–127 (2006)
45. J. de la Roche-Yepes, J.M. González, E. Restrepo-Parra, & H. Sánchez-Sthepa, Corrosion resistance and tribological behavior of WS₂-Ti coatings by Ti cathode power changes in magnetron co-sputtering. *Dyna*. **85**, 221–226 (2018)
46. Y. Yan, B. Xia, X. Qi, H. Wang, R. Xu, J.Y. Wang, H. Zhang, X. Wang, Nano-tungsten carbide decorated graphene as co-catalysts for enhanced hydrogen evolution on molybdenum disulfide. *Chem. Commun.* **49**, 4884–4886 (2013)
47. G. Yan, C. Wu, H. Tan, X. Feng, L. Yan, H. Zang, Y. Li, N-Carbon coated P-W₂C composite as efficient electrocatalyst for hydrogen evolution reactions over the whole pH range. *J. Mater. Chem. A*. **5**, 765–772 (2017)
48. Q. He, L. Wang, K. Yin, S. Luo, Vertically aligned ultrathin 1T-WS₂ nanosheets enhanced the electrocatalytic hydrogen evolution. *Nanoscale Res. Lett.* **13**, 1–9 (2018)
49. P.V. Sarma, C.S. Tiwary, S. Radhakrishnan, P.M. Ajayan, M.M. Shaijumon, Oxygen incorporated WS₂ nanoclusters with superior electrocatalytic properties for hydrogen evolution reaction. *Nanoscale*. **10**, 9516–9524 (2018)
50. W. Yang, J. Wang, C. Si, Z. Peng, J. Frenzel, G. Eggeler, Z. Zhang, [001] preferentially-oriented 2D tungsten disulfide nanosheets as anode materials for superior lithium storage. *J. Mater. Chem. A*. **3**, 17811–17819 (2015)
51. M.A. Ahmed, A.A.A. Shaweesh, N.M. El-Ashgar, I.M. El-Nahal, M.M. Chehimi, F. Babonneau, Synthesis and characterization of immobilized-polysiloxane monoamine-thiol triacetic acid and its diamine and triamine derivatives. *J. Sol-Gel. Sci. Technol.* **78**, 660–672 (2016)
52. S. Li, Z. Yao, J. Zhou, R. Zhang, H. Shen, Fabrication and characterization of WO₃ thin films on silicon surface by thermal evaporation. *Mater. Lett.* **195**, 213–216 (2017)
53. S.-K. Jerng, D.S. Yu, J.H. Lee, C. Kim, S. Yoon, S.H. Chun, Graphitic carbon growth on crystalline and amorphous oxide substrates using molecular beam epitaxy. *Nanoscale Res. Lett.* **6**, 1–6 (2011)
54. P. Connor, J. Schuch, B. Kaiser, W. Jaegermann, The determination of electrochemical active surface area and specific capacity revisited for the system MnO_x as an oxygen evolution catalyst. *Z. Phys. Chem.* **234**, 979–994 (2020)
55. J. Hu, B. Huang, C. Zhang, Z. Wang, Y. An, D. Zhou, H. Lin, M.K. Leung, S. Yang, Engineering stepped edge surface structures of MoS₂ sheet stacks to accelerate the hydrogen evolution reaction. *Energy Environ. Sci.* **10**, 593–603 (2017)

56. M.A. Tekalgne, K. Van Nguyen, D.L.T. Nguyen, V.H. Nguyen, T.P. Nguyen, D.V.N. Vo, Q.T. Trinh, A. Hasani, H.H. Do, T.H. Lee, Hierarchical molybdenum disulfide on carbon nanotube–reduced graphene oxide composite paper as efficient catalysts for hydrogen evolution reaction. *J. Alloys Compd.* **823**, 153897 (2020)
57. I.M. Mosa, S. Biswas, A.M. El-Sawy, V. Botu, C. Guild, W. Song, R. Ramprasad, J.F. Rusling, S.L. Suib, Tunable mesoporous manganese oxide for high

performance oxygen reduction and evolution reactions. *J. Mater. Chem. A.* **4**, 620–631 (2016)

Publisher's Note

Springer Nature remains neutral with regard to jurisdictional claims in published maps and institutional affiliations.

Submit your manuscript to a SpringerOpen[®] journal and benefit from:

- Convenient online submission
- Rigorous peer review
- Open access: articles freely available online
- High visibility within the field
- Retaining the copyright to your article

Submit your next manuscript at ► [springeropen.com](https://www.springeropen.com)